Ruthenate perovskite with face-sharing motifs for sustainable alkaline hydrogen evolution

David Shuk-Yin Tong (tongsy@cuhk.edu.cn)
The Chinese University of Hong Kong, Shenzhen https://orcid.org/0000-0003-3501-0455
Chuanhui Zhu
Sun Yat-Sen University
Hao Tian
The Chinese University of Hong Kong, Shenzhen
Pengfei Tan
Sun Yat-Sen University
Bin Huang
Sun Yat-Sen University
Shuang Zhao
Sun Yat-Sen University
Guo-Hong Cai
Sun Yat-Sen University
Chongyang Yuan
Sun Yat-Sen University
Mei-Huan Zhao
Sun Yat-Sen University
Meng Cao
The Chinese University of Hong Kong, Shenzhen
Jianfa Zhao
Institute of Physics, Chinese Academy of Sciences
Luchuan Shi
Chinese Academy of Sciences
Haili Song
Sun Yat-Sen University
Keke Huang
Jilin University
Shouhua Feng
Jilin University
Mark Croft
The State University of New Jersey
Chang-Qing Jin

Chinese Academy of Sciences

Man-Rong Li

Sun Yat-Sen University

Article

Keywords:

Posted Date: October 27th, 2023

DOI: https://doi.org/10.21203/rs.3.rs-3270649/v1

Additional Declarations: There is **NO** Competing Interest.

Abstract

Hydrogen-centered electrochemical technologies play a vital role in sustainable energy conversion and storage. One of the challenges in achieving cheap hydrogen is to bridge the gap between advanced electrocatalysts and highly effective electrodes. Here, we synthesized $BaRuO_3$ in four polymorphs with distinct RuO_6 connections to rationalize the impact of crystal structure feature on transferable alkaline hydrogen evolution activity. The 9*R*-$BaRuO_3$ displays the best hydrogen evolution reaction activity and stability in alkaline solution with a small Tafel slope of 30 mV dec^{-1} and a low overpotential of $\eta_{10} < 51$ mV, which is comparable to Pt/C and superior to the most highly efficient ruthenium-based oxide hydrogen evolution catalysts reported to date. Such performance is ascribed to its high intrinsic activity that is delivered by the *d*-*d* interaction and optimal intermediate adsorption. More importantly, 9*R*-$BaRuO_3$ can be easily synthesized on a large scale as demonstrated by the 9*R*-$BaRuO_3$-500 g sample in this study. The high intrinsic activity and micron size of 9*R*-$BaRuO_3$ powders enable a successful performance transfer from a lab-based three-electrode system to a commercial alkaline electrolyser operated under industrial conditions. The findings presented here not only demonstrate a robust and efficient HER electrocatalyst for practical electrolysers, but also emphasize the effect of structural features in the design of advanced electrocatalysts.

Introduction

Increasing the share of clean sustainable energy is a top priority task faced by the broad scientific community, whereas the inherent spatial and temporal dependence of sustainable energy make it difficult to improve the market penetration. In this regard, green hydrogen production from water electrolysis represents an essential role for converting intermittent sustainable electricity into the chemical energy for flexible arrangements. Still, the large-scale application of hydrogen-centered electrochemical technologies is hindered by poor economics of green hydrogen caused by high power consumption. To boost the hydrogen economy, a key step is to increase water electrolysis efficiency and produce cheap hydrogen[1-3]. Among various water electrolysis technologies, the alkaline electrolyser (AEL) has been commercialized for more than 100 years, nevertheless, its performance is limited by the development of key materials, in particular the cathode catalyst. In alkaline media, the sluggish kinetics of hydrogen evolution reaction (HER) at cathode is one of the critical challenges[4-7]. Even as the state-of-art HER catalyst, Pt-based catalysts suffers a slow turnover rate as compared to that at acidic conditions, owing to the unfavorable water dissociation[8-11]. Considerable efforts have been dedicated to improving HER performance in the alkaline media[12-14]. While numerous nanocatalysts surpass the industry-used Ni in the three-electrode configuration (TEC) at laboratories, their performance can be hardly transferred to commercial electrolyser operated at industrial conditions[15-17]. To fabricate an advanced electrode in AEL, it generally requires platting the powder catalyst on a nickel net at elevated temperature, in which process the catalytic activity steaming from quantum size effect, facet-dependent effect as well as the other geometric structural benefits, are largely remove. It is, therefore, a standing challenge to realize the direct

transferability of catalysts' performance from laboratory conditions to practical electrolysers. Instead of geometric activity, this challenge calls for the high intrinsic activity of an HER catalyst to facilitate scaling up production and deliver transferable activity and stability.

The solid-state reaction is a promising route to enable scaled-up production of micron-sized oxides, providing a platform to investigate intrinsic activities that can be easily transferred to an industry electrode. In this work, we prepared four oxide barium ruthenates (9*R*-, 4*H*-, 6*H*- and 3*C*-$BaRuO_3$, BRO) and studied their performance in catalyzing alkaline HER. BROs are synthesized using the solid-state reaction and high-pressure/high-temperature (HPHT) method. The synthesis method assures repeatability of properties, and we can routinely obtain massive 500 g product that exhibits the same alkaline HER activities as laboratory-sized samples. Among the four polymorphs, the 9*R*-BRO phase displays a remarkable alkaline HER activity with a Tafel slope of 30 mV dec^{-1}, even smaller than that of the commercial catalyst Pt/C (34 mV dec^{-1}). The overpotential η (at current density 10 mA cm^{-2}) of the 9*R*-BRO phase is 51 mV, strikingly close to that of Pt/C. Critical to large-scale commercial applications, the price activity (A/$) of 9*R*-BRO is 8 and 48 times better than that of commercial Pt/C and nano-nickel even for hand-ground samples with an average cluster size of 2-4 microns. Equally important is the fact that the catalyst has been also used as the cathode of a commercial AEL, which can operate at 4,000 A/m^2 for 1.74 V, outperforming the most advanced commercial AEL systems.

To investigate why 9*R*-BRO has such exceptional alkaline HER activities and why its activities are better than that of the 4*H*-, 6*H*- and 3*C*-BRO phases, we carried out synchrotron powder X-ray analysis (SPXD), magnetic and electric measurements, and density functional theory (DFT) calculations to study the structural, electronic and magnetic properties of the four polymorphs. The basic building block of the polymorphs is the RuO_6 octahedron, and adjacent octahedra are stacked together in either face- or corner-shared configurations. Among the polymorphs, 9*R*-BRO has the highest/lowest percentage of face-shared/corner-shared octahedra (66%/34%), followed by 4*H*-BRO (50%/50%), 6*H*-BRO (34%/66%) and 3*C*-BRO (0/100%). Our analysis shows that in face-shared octahedra, there is direct *d*-*d* interaction leading to very strong Ru-Ru intermetallic bonding, which could promote electron transfer in water reduction. We further find that H* species, formed at bridge-oxygen sites of surface face-shared octahedra, possess adsorption free energy (ΔG_{H*}) very close to zero (the optimal in a volcano plot), resulting in superior HER activities. As 9*R*-BRO has the highest percentage of such sites, its HER efficiency should be superior among the polymorphs as we observed.

Results and discussion

Synthesis and crystal structure characterization of $BaRuO_3$. Four $BaRuO_3$ polymorphs with distinct crystal structures are synthesized by elevated synthetic pressure as elaborated in the experimental section and schematically shown in Fig. 1a. The quality and purity of the four different polymorphs (9*R*-, 4*H*-, 6*H*- and 3*C*-BRO) are assessed by SPXD measurements (Fig. 1b-e). The diffraction peaks are well matched with those of the pure phases, confirming high fidelity synthesis and phase transitions of

$BaRuO_3$[18,19]. Compared to conventional laboratory PXD, SPXD provides higher sensitivity and better resolution, thus improving the identification of crystalline structures. Detailed crystallographic data with selected atomic distances, bond angles, and calculated bond valence sums (BVS) are listed in **Supplementary Tables S1** and **S2**. The obtained data further confirm that the as-prepared $BaRuO_3$ is without trace impurities. At ambient pressure, 9*R*-BRO is the thermodynamically stable phase. It adopts a rhombohedral (*R*-3*mH*) structure with Ru_3O_{12} trimers formed by three face-shared RuO_6 octahedra. The Ru_3O_{12} trimers are connected to each other by corner-sharing oxygen atoms (Fig. 1a, left). At an elevated synthesis pressure of 3 GPa, the number of corner-shared octahedra increases and results in a reconstructive phase transition to the hexagonal 4*H*-BRO ($P6_3/mmc$) structure (Fig. 1a, middle left). The basic building blocks are Ru_2O_9 dimers corner-sharing with neighbor Ru_2O_9 dimers. Further increasing the synthesis pressure to 5 GPa yields a second hexagonal structure 6H-BRO ($P6_3/mmc$) with the appearance of new corner-connected structures comprising Ru_2O_9 dimers with RuO_6 octahedral layers (Fig. 1a, middle right). Finally, the cubic perovskite structure 3C-BRO (*Pm*-3*m*, Fig. 1a, right) containing only corner-shared RuO_6 octahedra is synthesized at 18 GPa. Here we measured only key information for 3*C*-BRO because of its extremely harsh synthesis condition (18 GPa) and poor yield (~ 5 mg each batch). The as-prepared four samples have diverse crystal structures and comparable micron-size, providing a rich platform to study the correlation between structural feature and intrinsic catalytic activity.

The crystal structures of the polymorphs are further corroborated by high-resolution transition electron microscope (HRTEM, **Figure S1**), where lattice fringes match well with lattice spacings of the different polymorphs. Energy-dispersive x-ray (EDX) elemental-mapping data confirm the elemental composition and homogeneous distribution of the as-synthesized oxides (**Figure S2**). From scanning electron microscopy (SEM) images, comparable micro-meter-sized particles are observed in the as-synthesized oxides (**Figure S3**). Their bulk nature is further confirmed by a rather small surface area calculated from Brunauer-Emmett-Teller (BET) measurements (**Figure S4**). X-ray photoelectron spectroscopy (XPS) is carried out to evaluate the chemical composition and oxidation state of the oxides. As displayed in **Figure S5**, the Ba 3*d* and Ru 3*p* spectra in all samples are the same, indicating that only Ba^{2+} and Ru^{4+} ions exist in the as-synthesized oxides and the oxygen stoichiometry of the oxides is uniform. The similar valence states of 4*H*-, 6*H*-and 3*C*-BRO can also be seen in the results of BVS calculations (**Supplementary Table S2**). X-ray absorption near-edge spectroscopy (XANES, **Figure S6**) is employed to finally determine the valence state of Ru. The standard double-perovskite Ca_2YRuO_6, which has a $4d^4$-Ru^{5+} configuration[20–22], possesses a double peak feature: (t_{2g}-hole related) and (e_g-hole related) (**Figure S6**). The XANES data for 9*R*-, 4*H*-, 6*H*- and 3*C*-BRO show a single peak, typical of the $4d^4$-Ru^{4+} configuration. To sum up, the pure phase and bulk nature of as-made $BaRuO_3$ polymorphs provide an ideal platform to investigate the structure features of ruthenates and their correlated intrinsic activity on HER.

Assessment of alkaline HER performance. Alkaline HER activities of different BRO polymorphs are collected and compared in this study. In addition, micro-meter RuO_2, nano-nickel (~ 20–100 nm) and nano-Pt/C catalysts used in commercial applications are chosen as benchmarks to assess the

performance of the as-synthesized micro-sized BROs. Figure 2a shows the linear sweep voltammetry (LSV) polarization curves of the catalysts in the potential range of -0.3 to 0.1 V versus the reversible hydrogen electrode (RHE). Except for Pt/C, 9*R*-BRO outperforms all control samples in terms of overpotential η at 10 mA cm^{-2}. It only requires 51 mV for 9*R*-BRO to reach 10 mA cm^{-2}, which is substantially lower than that of 4*H*-BRO (89 mV), 6*H*-BRO (118 mV), 3*C*-BRO (143 mV), nano-nickel (362 mV), and RuO_2 (69 mV), and strikingly close to that of Pt/C (42 mV). An important electrochemical kinetic parameter is the Tafel slope, with a smaller Tafel slope signaling faster kinetics[23–25]. As shown in Fig. 2b, the Tafel slopes are 30, 69, 79, 97 mV dec^{-1} for 9*R*-, 4*H*-, 6*H*- and 3*C*-BRO, respectively, indicating that 9*R*-BRO possesses the best electron transport rate among the four polymorphs. More significant is the fact that the Tafel slope of 9*R*-BRO is even smaller than that of Pt/C (34 mV dec^{-1}). Overall, the overpotential @ 10 mA cm^{-2} of 9*R*-BRO is among the most efficient of all ruthenium-based oxides for alkaline HER activities reported to date, even better than that of most nano-structured benchmark catalysts that are more expensive to prepare (Fig. 2c). Considering the hand-ground nature of the 9*R*-BRO sample and relatively low surface area deduced from BET calculations, the high HER activities must be ascribed to its extremely powerful intrinsic activity. In **Figure S7** the activity normalized to BET surface area, it also can be seen that the activity per surface area of 9*R*-BRO is superior among the polymorphs, highlighting its superior intrinsic activity again.

To assess the commercial potential of 9*R*-BRO, specific mass activity (A/g) is a vital criterion. As shown in Fig. 2d, despite its low surface area, the specific mass activity of 9*R*-BRO is 180.3 A/g, which is 2 times higher than that of (commercial) micro-RuO_2 (97.4 A/g) and 1.3 times higher than that of (commercial) nano-Pt/C (137.8 A/g). For the all-important specific price activity (A/$) indicator, 9*R*-BRO is 10 and 8 times better than that of micro-RuO_2 and nano-Pt/C, respectively. Nickel-based electrodes are widely used in commercial AEL. We compare the performance of 9*R*-BRO with that of nano-nickel under identical conditions. The overpotential η at 10 mA cm^{-2} is 51 mV (9*R*-BRO) versus 362 mV (nano-nickel) as shown in Fig. 2a. The Tafel slope is 30 mV dec^{-1} (9*R*-BRO) versus 164 mV dec^{-1} (nano-nickel) in Fig. 2b. The specific mass activity (A/g) is 180.3 (9*R*-BRO) versus 2.9 (nano-nickel) and the specific price activity (A/$) is 33.4 (9*R*-BRO) versus 0.7 (nano-nickel), a factor of 48 times better (Fig. 2d and **Table S3**). These figures indicate that 9*R*-BRO could replace Ni for commercial use in alkaline HER electrolysers. In terms of scalability, 9*R*-BRO is synthesized by solid-state reaction, a technique commonly used in the industrial production of $LiFePO_4$ and $LiCoO_2$ for cathode materials in lithium batteries. The synthesis of micron-sized oxides by this technique has a proven record of repeatability. As a demonstration, we have prepared a massive 500 g sample (hereafter denoted as 9*R*-BRO-500) by scaled-up synthesis. The massive sample displays identical alkaline HER activities as laboratory-sized samples (Fig. 3a). Another test necessary for the development of a commercial catalyst is its performance under large current densities typically reached in commercial systems. We plated the 9*R*-BRO powder on a nickel net ($d \sim 5.5$ cm; left inset in Fig. 3b) used as the cathode of a commercial AEL of 0.5 Nm^3/h capacity. As displayed in Fig. 3b, we obtained an operating cell voltage of ~ 1.74 V at a current density of 4,000 A/m^2, which outperforms figures published in the most advanced commercial AEL systems (the normally quoted cell voltages in

most commercial systems are over 1.9 V). We thus expect that 9*R*-BRO can easily undergo further optimizations as a cathode catalyst in commercial AEL systems.

The long-term operational stability of catalysts is another critical aspect in practical applications. As shown in Fig. 3c, a slight fluctuation of current density is observed over 40 hours of operation at an overpotential of 50 mV. The durability of the catalyst is further confirmed by 1,000 continuous cyclic voltammetry (CV) analyses. The 9*R*-BRO sample, being the thermodynamically stable phase at ambient pressure, exhibits superior structural stability over the other polymorphs (**Figure S8**). Noteworthy, the AEL system with 9*R*-BRO also demonstrates considerable stability under industrial conditions in ~ 30 hours (Fig. 3d), emphasizing the excellent application potential of 9*R*-BRO in achieving cheap hydrogen. One can ascribe this to the more robust structure feature of face-shared RuO_6 octahedral proportion for which 9*R*-BRO has the highest percentage. It is not easy to break apart two face-shared octahedra unless one breaks three nearest neighbor Ru-O bonds. To further assess the structural stability of 9*R*-BRO, we compare the PXD and XPS data before and after the 1,000 cycles of voltammetry operation. We also place the oxide in a harsh media (1 M KOH and 1 M HCl) for two weeks (**Figure S9**). We observe no apparent change in the XRD and XPS data pre- and post-treatments, indicating that the superior stability of 9*R*-BRO.

The correlation between crystal structure feature and alkaline HER activity. Bulk conductivity could be a critical criterion to affect catalytic performance. In **Figure S10**, the partial density of states (PDOS) is calculate, showing that all the as-made oxides are metallic[26]. Experimentally, the temperature-dependent electrical resistivities of 9*R*-, 4*H*-, and 6*H*-BRO are measured (**Figure S11**). All three polymorphs exhibit low resistivity at the same order of magnitude at room temperature. In addition, previous work has shown that 3*C*-BRO displays a similar resistivity behavior[27]. The metallic behavior of all four polymorphs is beneficial to electron transportation and thus the HER rate.

To explain the substantial activity discrepancy shown by different polymorphs, structural analysis of the four $BaRuO_3$ polymorphs is counted on and shown in **Figure S12**, where the subscripts “F” and “C” denote face- and corner-shared atoms, respectively. Diverse crystal structures of BROs consist of distinct RuO_6 connections. Specifically, the cubic perovskite structure of 3*C*-BRO contains only corner-shared RuO_6 octahedra, and the other three polymorphs consist of different proportions of face/corner-shared RuO_6 octahedra. It is worth noting that, as displayed in **Figure S13b**, the Ru-Ru bond distance in face-shared RuO_6 octahedra of 9*R* (2.53 Å), 4*H* (2.55 Å) and 6*H* (2.57 Å) is smaller than the nearest neighbor Ru-Ru distance in Ru metal (2.65 Å). This is a sign of exceptionally strong intermetallic bond formation caused by direct Ru-*d*/Ru-*d* interaction in the ruthenates[28–30]. It is expected that different RuO_6 connections can alter the electron exchange interaction mode between metal atoms[19]. The magnetic properties of oxides are good indicators of the interaction of the Ru 4*d* orbitals. The nearest-neighbor exchange interaction in face-shared octahedra is direct electron hopping across the 180° Ru-Ru bond, leading to antiferromagnetic (AFM) behavior. In corner-shared octahedra, electron hopping between Ru ions mediated by an O ion should produce ferromagnetic (FM) behavior[19]. As there is no obvious deviation

between zero-field-cooled (ZFC) and field-cooled (FC) data of these oxides, in Fig. 4a, we only show the ZFC mode data. With the decrease in faced-shared and increase in corner-shared octahedral proportion in these polymorphs, the magnetic behaviors of BRO demonstrate systematic alteration from the antiferromagnetic behavior (9*R*-BRO) to ferromagnetic behavior (9*R*-BRO). The measured magnetic properties agree well with the expected electronic exchange interaction in the different polymorphs. Taken together, more face-shared oligomer gives shorter Ru-Ru bond with direct *d-d* interaction.

More DFT calculations are performed to further elucidate the effect of Ru-Ru interaction. First, we use the crystal orbital Hamiltonian population (COHP) results (Fig. 4b) to establish that in bulk crystals, the Ru-Ru bonding orbitals of face-shared octahedra reside in the range between − 5.8 to -7.8 eV (the pink range) below E_F. Mapping the PDOS in real space at this energy window (see Fig. 4b**)** shows that the Ru-Ru bonding orbitals connect face-shared octahedra in typical 9*R*-BRO. Given the *d-d* interaction in the face-shared octahedra, the electron could hop back and forth between the face-shared Ru atoms with enhanced itinerant[31–33], promoting electron transfer in the crystal. In addition to charge transportation, hydrogen release is another important step in determining HER efficiency after water dissociation. Water dissociation generates *OH that anchors on the surface Ru and releases H* to vicinal O* atoms. Through a Tafel or Heyrovsky step, the adsorbed H* then forms H_2 molecules and leaves the surface. In this process, the adsorption-free energy of H* (ΔG_{H*}) is a key descriptor, with a ΔG_{H*} value close to zero indicating a superior HER activity[34–36]. On the BRO surface, there are two types of oxygen sites: O_T or O_B (see **inset of** Fig. 4c), where the O_T can be found in both face- and corner-shared RuO_6 octahedra, O_B are present only in face-shared octahedra. At O_T sites, the values of ΔG_{H*} are too large to favor easy hydrogen evolution from O_TH* species. On the other hand, ΔG_{H*} at O_B sites are small, favoring HER. As shown in Fig. 4c, ΔG_{H*} for O_BH* is small, being less than |0.15 eV| for the 9*R*-, 4*H*- and 6*H*- polymorphs. For 9*R*-BRO, its ΔG_{H*} is close to the top of the volcano plot (optimal value), being − 0.01 eV. It is also noteworthy that 9*R*-BRO has the highest proportion of O_B sites. The values of ΔG_{H*} for O_BH* sites suggest that HER activities should be highest for the 9*R*-polymorph, followed by 4*H*- and 6*H*-BRO, in the order found by the experiment. To sum up, the correlation between *d-d* interaction intensity and HER activity can be seen in Fig. 4d, where the overpotential of BRO polymorphs sharply decreases with increasing proportions of face-shared RuO_6 octahedra in a sequence of 3*C*, 6*H*, 4*H* and 9*R*, as the face-sharing Ru-O linkage increases from 0% (in 3*C*-BRO) to 33% (in 6*H*-BRO), 50% (in 4*H*-BRO), and finally to 66% (in 9*R*-BRO). These results highlight the merits of 9*R*-BRO in delivering excellent catalytic reactivity in alkaline HER, consistent with experimental observations.

Conclusions

In summary, four $BaRuO_3$ polymorphs with distinct crystal and electronic structures were synthesized using solid-state reaction. Combining detailed structure analysis and theoretical calculations, we find that the *d-d* interaction rooted in the face-sharing motifs largely enable the high intrinsic activity of the 9*R*-$BaRuO_3$. Additionally, the 9*R*-$BaRuO_3$ can be easily synthesized in large scale as demonstrated by the 9*R*-

$BaRuO_3$-500 sample in this study. The high intrinsic activity and ease in scaled up production jointly endow 9*R*-$BaRuO_3$ powders as a transferable candidate from lab-based three-electrode system to a commercial alkaline electrolyser operated under industrial conditions. It is expected that the further optimization of 9*R*-$BaRuO_3$ will fully unleash the potential of this material as an advanced cathode catalyst in alkaline electrolysers to achieve the goal of cheap hydrogen.

Methods

Synthesis of $BaRuO_3$. Ruthenium metal (Ru, 99.9%) and barium carbonate ($BaCO_3$, 99.95%) powder used in this work were ordered from Aladdin Ltd. (Shanghai, China). The pure 9*R*-BRO phase was synthesized by the solid-state reaction method at ambient pressure. Stoichiometric amounts of Ru and $BaCO_3$ were weighed, mixed and ground in an agate mortar, then the powder was calcined at 900 ℃ in air for 12 h. The obtained powder was ground and fired at 1100 ℃ for 40 h, with an intermediate and a final grinding. The grinding was done manually and lasted at least 30 minutes. To obtain the other polymorphs, higher pressures at 1000 ℃ are needed. The powder of 9*R*-BRO was placed in a Pt capsule and subjected to 3–18 GPa at 1000 ℃ for 30 minutes in a Walker-type multi-anvil high-pressure apparatus. The sample was quenched to room temperature, followed by slow pressure decompression. The 4*H*-, 6*H*- and 3*C*-phases were prepared at 3, 5 and 18 GPa, respectively. These samples obtained under high pressures are in pellet form and were ground to powder.

Basic characterizations. PXD using the Rigaku (D-MAX 2200 VPC) instrument with a Cu-Kα radiation source (λ = 1.5418 Å) and SPXD using the beamline BL14B (λ = 0.68993 and 0.69260 Å) at the Shanghai Synchrotron Radiation Facility (SSRF) were used to determine the crystal structures of the polymorphs. The TOPAS software was used to produce detailed crystallographic data listed in Tables S1 and S2[37]. Morphology and microstructure were characterized using SEM (Phenom XL) and HRTEM (JEM-ARM200P). The oxidation state was investigated by XPS spectra (ESCALab250). The XANES data were collected in the total electron yield mode, at the Brookhaven National Synchrotron Light Source (NSLS-II) on beamline 7-ID SSA-2 using a Si (111) double crystal monochromator. The magnetic measurements were performed by the Magnetic Property Measurement System (MPMS3) in the temperature range between 10–300 K. The susceptibility is evaluated in both ZFC and FC modes under an applied filed of 1 T. Temperature dependent resistivity measurements were performed by the conventional four-probe technique in the temperature range 10–300 K using a Physical Property Measurements System (PPMS) from Quantum Design.

Electrochemical measurements. The electrochemical performance of the polymorphs was evaluated in a standard three-electrode configuration using an electrochemical workstation (CHI760D). The Hg/HgO electrode and graphite rod were used as reference and counter electrodes, respectively. Working electrodes for HER measurements were prepared as follows: 5 mg of catalyst and 40 µL of 5 wt % Nafion were dispersed in 5 mL ethanol followed by sonication, then 20 µL of the catalyst ink was dropped on the glassy carbon electrode (0.283 $mg.cm^{-2}$) and dried at room temperature before electrocatalytic tests. No

carbon was added to the catalyst ink to exclude any effect of carbon presence on the HER process. The HER measurements were carried out in a 1 M KOH solution. For equal comparison, a reversible hydrogen electrode (RHE) was used for calibration of the HER measurements: $E_{RHE} = E_{Hg/HgO} + 0.059 \times pH + 0.098$. The scan rate for the polarization curves is 5 mV s^{-1}, and stability tests of the different polymorphs were conducted through continuous CV measurements for 1000 cycles at a rate of 100 mV s^{-1}.

Computational details. The adsorption geometry and adsorption energy were investigated by using DFT calculations with a 520 eV cutoff for the plane-wave basis set. To represent nuclei and core electrons, the projected augmented wave method was employed as implemented in the Vienna Ab-initio Simulation Package[38–40]. The electron exchange-correlation was described by using the Perdew-Burke-Ernzerhof (PBE) form of the generalized gradient approximation (GGA)[41,42]. The DOSs were calculated by using spin-polarized DFT including on-site Coulomb corrections on the Ru 4*d* electrons with fixed values of U_{Ru} = 2.3 eV, as adopted in prior works.

Declarations

Data availability

All data that support the findings in the current study are available within the Article and its Supplementary Information. Source data are available from the corresponding authors upon reasonable request.

Acknowledgements

This work was financially supported by the National Science Foundation of China (Grant No. 22090041 and 12174326), the Program for Guangdong Introducing Innovative and Entrepreneurial Teams (Grant No. 2017ZT07C069 and 2019ZT08L101), the Guangdong Basic and Applied Basic Research Foundation (Grant No. 2022B1515120014), the National Key R&D Program of China (2018YFA0305700), Shenzhen Natural Science Foundation (Grant No. GXWD20201231105722002- 20200824163747001), Shenzhen Key Laboratory of Eco-materials and Renewable Energy (Grant No. ZDSYS20200922160400001). The XANES were performed by Conan Weiland (NIST) on NSLS-II beamline 7-ID-2 SST-2 and supported in part under DOEBES (DE-SC0012704). The authors thank the National Supercomputer Center in Guangzhou, and the staffs from BL14B and BL15U1 at Shanghai Synchrotron Radiation Facility for assistance during data collection.

Author contributions

C. Zhu designed and performed the experiments. H. Tian performed theoretical calculations. P. Tan, B. Huang, G.-H. Cai, C. Yuan and M. Cao performed the catalyst synthesis and electrochemical experiments. S. Zhao conducted the magnetic and resistivity measurements. M.-H. Zhao carried out the SEM measurements. L. Shi, J. Zhao and C.-Q. Jin synthesized the 3*C*-BRO. H. Song carried out the HRTEM measurement. M. Croft performed the XANES characterization. K. Huang and S. Feng collected the XPS

data. C. Zhu and H. Tian draft the original manuscript. S.-Y. Tong and M.-R. Li supervised the project and polished the manuscript. All the authors discussed the results and revised the manuscript.

Competing interests

The authors declare competing interests.

References

1. Lagadec, M. F. & Grimaud, A. Water electrolysers with closed and open electrochemical systems. Nat. Mater. 19, 1140–1150 (2020).
2. Chu, X. et al. Structural design and performance research of methanol steam reforming microchannel for hydrogen production based on mixing effect. Int. J. Hydrogen Energ. 45, 20859–20874 (2020).
3. Kitano, M. et al. Ammonia synthesis using a stable electride as an electron donor and reversible hydrogen store. Nat. Chem. 4, 934–940 (2012).
4. Liu, E. et al. Unifying the hydrogen evolution and oxidation reactions kinetics in base by identifying the catalytic roles of hydroxyl-water-cation adducts. J. Am. Chem. Soc. 141, 3232–3239 (2019).
5. Ledezma-Yanez, I. et al. Interfacial water reorganization as a pH-dependent descriptor of the hydrogen evolution rate on platinum electrodes. Nat. Energy 2, 17031 (2017).
6. Wang, X. et al. Strategies for design of electrocatalysts for hydrogen evolution under alkaline conditions. Mater. Today 36, 125–138 (2020).
7. Anantharaj, S. et al. Strategies and Perspectives to Catch the Missing Pieces in Energy-Efficient Hydrogen Evolution Reaction in Alkaline Media. Angew. Chem. Int. Ed. 60, 18981–19006 (2021).
8. Zhu, S. et al. The role of ruthenium in improving the kinetics of hydrogen oxidation and evolution reactions of platinum. Nat. Catal. 4, 711–718 (2021).
9. Li, M. et al. Single-atom tailoring of platinum nanocatalysts for high-performance multifunctional electrocatalysis. Nat. Catal. 2, 495–503 (2019).
10. Zhang, J. et al. Single platinum atoms immobilized on an MXene as an efficient catalyst for the hydrogen evolution reaction. Nat. Catal. 1, 985–992 (2018).
11. Hansen, J. N. et al. Is there anything better than Pt for HER? ACS Energy Lett 6, 1175–1180 (2021).
12. She, S. et al. Efficient water splitting actualized through an electrochemistry-induced hetero-structured antiperovskite/(oxy)hydroxide hybrid. Small 16, e2006800 (2020).
13. Zhang, X. et al. Lithiation-induced amorphization of $Pd_3P_2S_8$ for highly efficient hydrogen evolution. Nat. Catal. 1, 460–468 (2018).
14. Sun, Y. et al. Modulating electronic structure of metal-organic frameworks by introducing atomically dispersed Ru for efficient hydrogen evolution. Nat. Commun. 12, 1369 (2021).

15. Yang, Y. et al. Electrocatalysis in Alkaline Media and Alkaline Membrane-Based Energy Technologies. Chem. Rev. 122, 6117–6321 (2022).
16. Zhang, W. et al. Water Electrolysis toward Elevated Temperature: Advances, Challenges and Frontiers. Chem. Rev. 123, 7119–7192 (2023).
17. Liu, R. T. et al. Recent advances in proton exchange membrane water electrolysis. Chem. Soc. Rev. 52, 5652–5683 (2023).
18. Zhao, J. G. et al. Structural and physical properties of the 6*H* $BaRuO_3$ polymorph synthesized under high pressure. J. Solid State Chem. 180, 2816–2823 (2007).
19. Jin, C. Q. et al. High-pressure synthesis of the cubic perovskite $BaRuO_3$ and evolution of ferromagnetism in $ARuO_3$ (*A* = Ca, Sr, Ba) ruthenates. P. Natl. Acad. Sci. USA 105, 7115–7119 (2008).
20. Zhu, C. et al. Pressure-induced intermetallic charge transfer and semiconductor-metal transition in two-dimensional $AgRuO_3$. CCS Chem. 5, 934–94 (2023).
21. Tan, X. et al. $MnFe_{0.5}Ru_{0.5}O_3$: an above-room-temperature antiferromagnetic semiconductor. J. Mater. Chem. C 7, 509–522 (2019).
22. Deng, Z. et al. Dynamic ferrimagnetic order in a highly distorted double perovskite Y_2CoRuO_6. Chem. Mater. 30, 7047–7054 (2018).
23. Song, F. & Hu, X. Ultrathin cobalt-manganese layered double hydroxide is an efficient oxygen evolution catalyst. J. Am. Chem. Soc. 136, 16481–16484 (2014).
24. Zhu, C. et al. Intersite charge transfer enhanced oxygen evolution reactivity on A_2IrO_3 (*A* = Li, Na, Cu) delafossite electrocatalysts. J. Electrochem. Soc. 169, 056523 (2022).
25. Zhu, Y. et al. Unusual synergistic effect in layered Ruddlesden-Popper oxide enables ultrafast hydrogen evolution. Nat. Commun. 10, 149 (2019).
26. Zhu, C. et al. Boosting oxygen evolution reaction by enhanced intrinsic activity in Ruddlesden-Popper iridate oxides. Chem. Eng. J. 423, 130185 (2021).
27. Lee, S. A. et al. Epitaxial Stabilization of Metastable 3*C* $BaRuO_3$ Thin Film with Ferromagnetic Non-Fermi Liquid Phase. Adv. Electron. Mater. 7, 2001111 (2021).
28. Lin, G. et al. Intrinsic electron localization of metastable MoS_2 boosts electrocatalytic nitrogen reduction to ammonia. Adv. Mater. 33, e2007509 (2021).
29. Kayser, P. et al. Thermal expansion in $BaRuO_3$ perovskites - an unusual case of bond strengthening at high temperatures. Dalton T. 46, 2974–2980 (2017).
30. Injac, S. D. A., Xu, Y., Denis Romero, F. & Shimakawa, Y. Pauli-paramagnetic and metallic properties of high pressure polymorphs of $BaRhO_3$ oxides containing Rh_2O_9 dimers. Dalton Trans. 50, 4673–4679 (2021).
31. Streltsov, S. V. & Khomskii, D. I. Covalent bonds against magnetism in transition metal compounds. P. Natl. Acad. Sci. USA 113, 10491–10496 (2016).

32. Li, N. et al. Identification of the active-layer structures for acidic oxygen evolution from 9*R*-$BaIrO_3$ electrocatalyst with enhanced iridium mass activity. J. Am. Chem. Soc. 143, 18001–18009 (2021).
33. Yang, L. et al. Efficient oxygen evolution electrocatalysis in acid by a perovskite with face-sharing IrO_6 octahedral dimers. Nat. Commun. 9, 5236 (2018).
34. Liu, Y. et al. Self-optimizing, highly surface-active layered metal dichalcogenide catalysts for hydrogen evolution. Nat. Energy 2, 17127 (2017).
35. Guan, D. et al. Searching general sufficient-and-necessary conditions for ultrafast hydrogen-evolving electrocatalysis. Adv. Funct. Mater. 29, 1900704 (2019).
36. Mahmood, N. et al. Electrocatalysts for hydrogen evolution in alkaline electrolytes: mechanisms, challenges, and prospective solutions. Adv. Sci. 5, 1700464 (2018).
37. Coelho, A. A. TOPAS and TOPAS-Academic: an optimization program integrating computer algebra and crystallographic objects written in C plus. J. Appl. Crystallogr. 51, 210–218 (2018).
38. Blochl, P. E. Projector augmented-wave method. Phys. Rev. B 50, 17953–17979 (1994).
39. Kresse, G. & Hafner, J. Ab initio molecular dynamics for liquid metals. Phys. Rev. B 47, 558–561 (1993).
40. Kresse, G. & Furthmuller, J. Efficient iterative schemes for ab initio total-energy calculations using a plane-wave basis set. Phys. Rev. B 54, 11169–11186 (1996).
41. Perdew, J. P., Burke, K. & Ernzerhof, M. Generalized Gradient Approximation Made Simple. Phys. Rev. Lett. 77, 3865–3868 (1996).
42. Grimme, S., Antony, J., Ehrlich, S. & Krieg, H. A consistent and accurate ab initio parametrization of density functional dispersion correction (DFT-D) for the 94 elements H-Pu. J. Chem. Phys. 132, 154104 (2010).

Figures

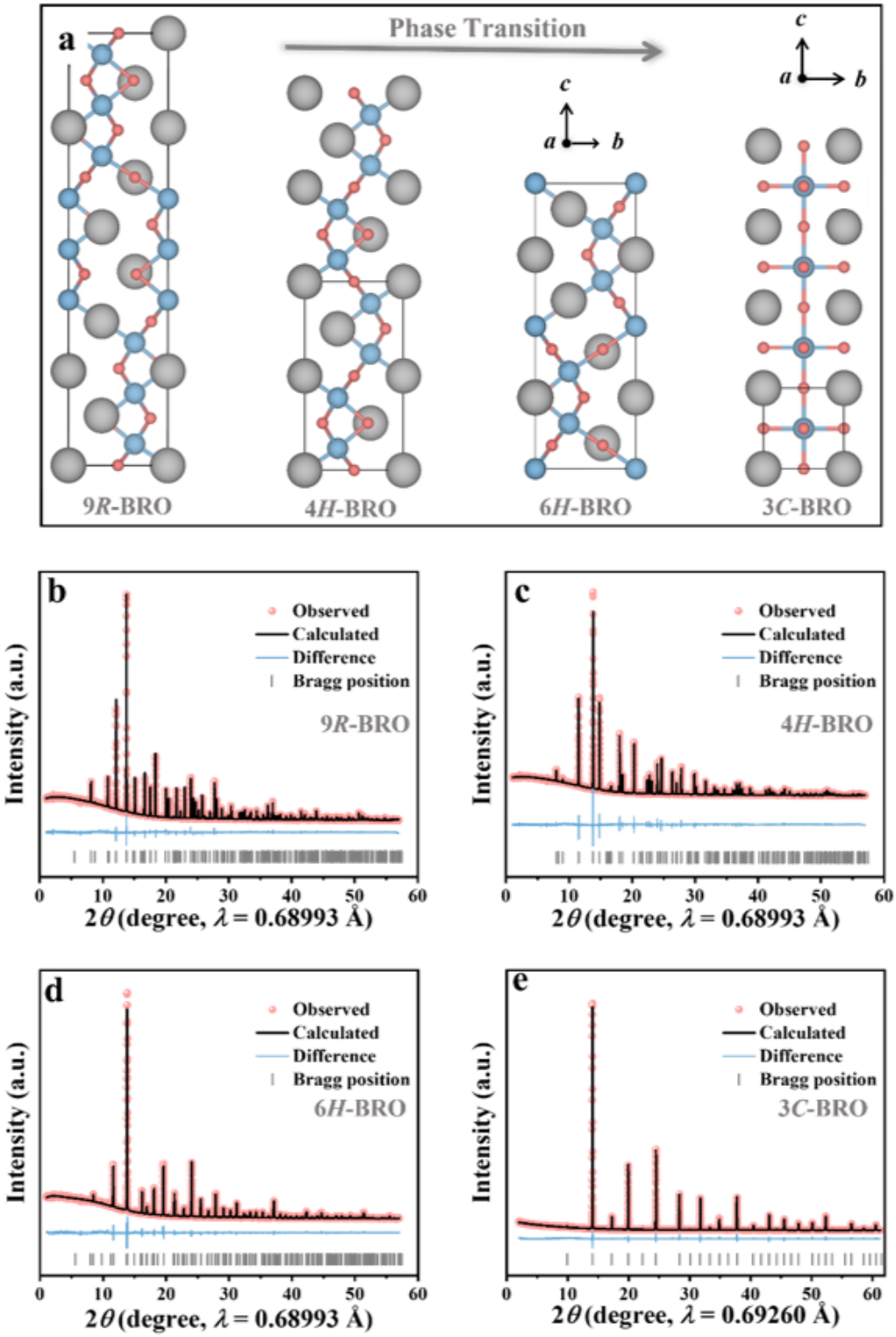

Figure 1

Structural characterization of the $BaRuO_3$ polymorphs. a, Pressure-dependent structural transition of $BaRuO_3$ showing 9*R*-, 4*H*-, 6*H*- and 3*C*- polymorphs. The direction of view for 9*R*-, 4*H*- and 6*H*- is [2$\bar{1}\bar{1}$], and for 3*C*- is [$\bar{1}$00]. Surfaces are formed in the (0$\bar{1}\bar{1}$) plane for 9*R*-, 4*H*- and 6*H*- polymorphs and (010) plane for the 3*C*- polymorph; **b,** SPXD data of 9*R*-BRO; **c** 4*H*-BRO; **d** 6*H*-BRO; and **e** 3*C*-BRO refined through the

TOPAS software; Experimental, calculated, difference curves and peak positions are shown in red, black, blue, and gray, respectively.

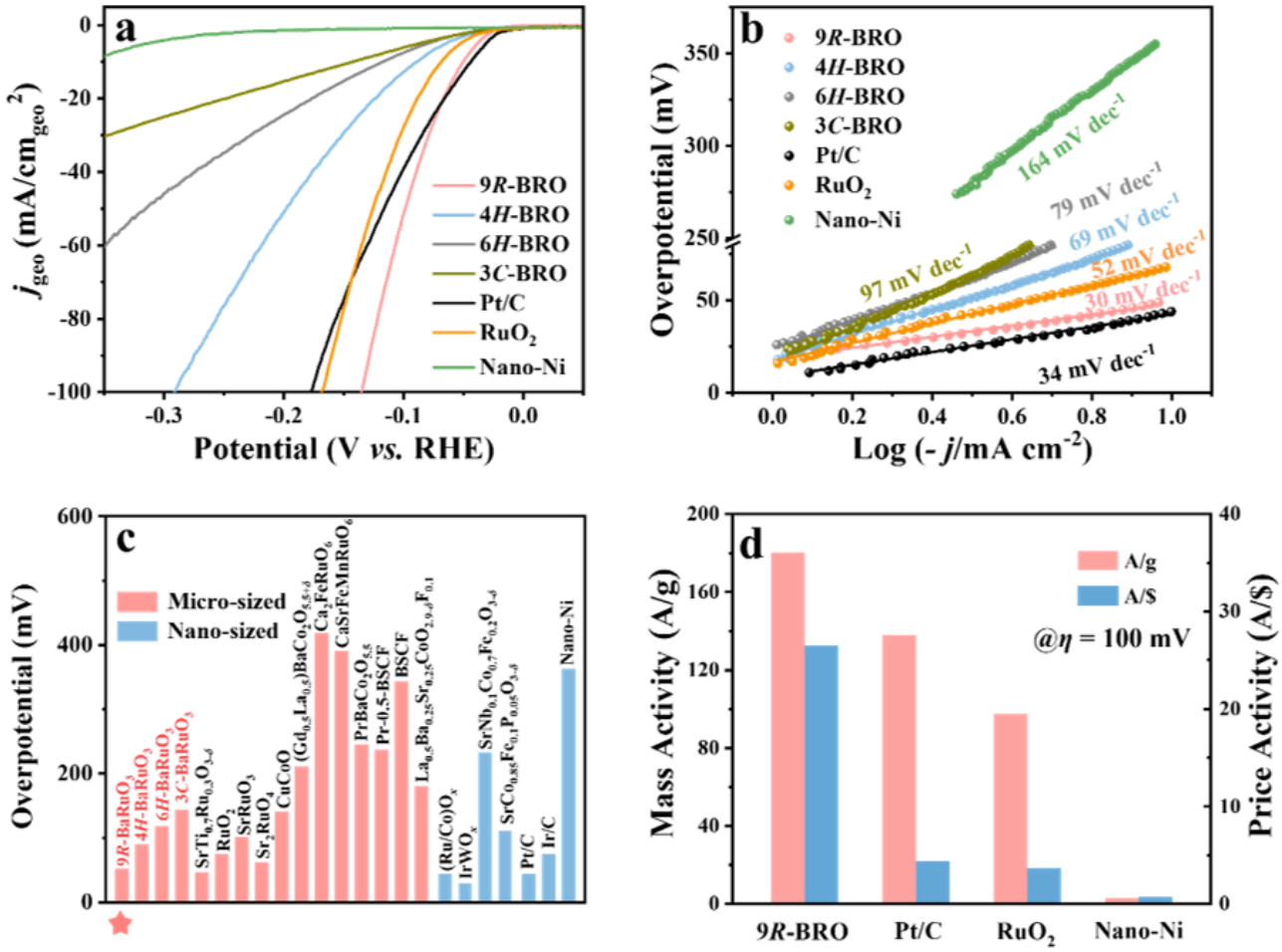

Figure 2

Electrocatalytic performance for different polymorphs of $BaRuO_3$ and reference HER catalysts. a, Comparison of the polarization curves of different BRO-polymorphs, commercial RuO_2 (HWRK), Pt/C (MACLIN) and nano-Ni (MACLIN) measured in 1 M KOH solution, cm_{geo}^2 represents geometric area. **b,** Corresponding Tafel plots of the different catalysts in 1 M KOH solution. **c,** Comparison of the overpotential @-10 mA cm^{-2} among the micron-sized and nano-sized oxides and other benchmark catalysts for alkaline HER activity. **d,** Specific mass activity (A/g) and price activity (A/$) for different catalysts at overpotential of η = 100 mV in 1 M KOH solution.

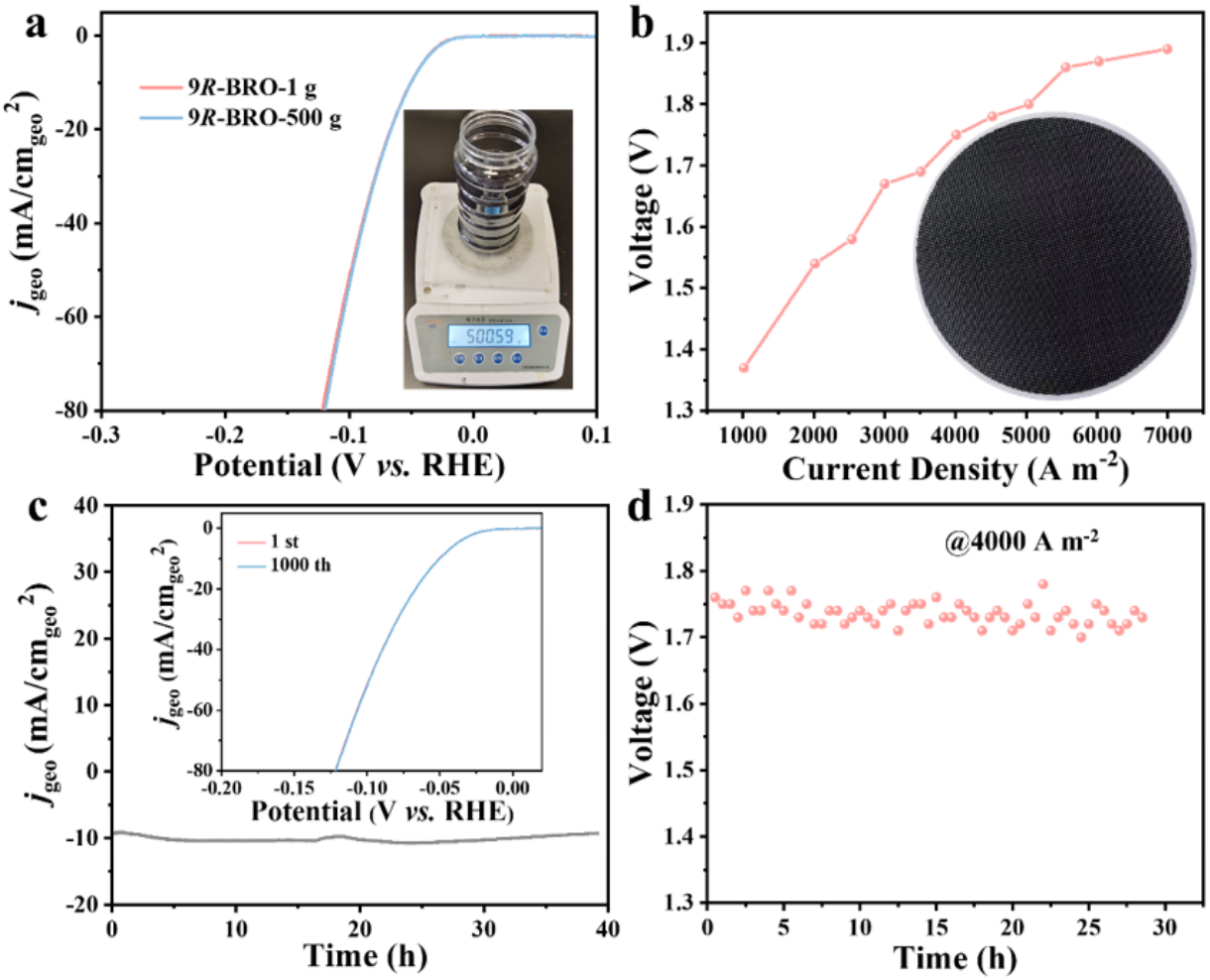

Figure 3

The application potential of 9*R*-BRO. a, Polarization curves of 9*R*-BRO 1 g sample and 9*R*-BRO-500 sample measured in 1 M KOH solution. **b,** Polarization curve of 9*R*-BRO powder plated on a nickel net used as cathode of a commercial alkaline electrolyser of 0.5 Nm^3/h capacity. **c,** Chronoamperometry curve of 9*R*-BRO at -0.05 V *vs.* time (RHE) and polarization curve after single and 1,000 cycles of voltammetry (CV) operation. **d,** Chronopotentiometry curve of the AEL using 9*R*-BRO operated at ~4000 A m^{-2}.

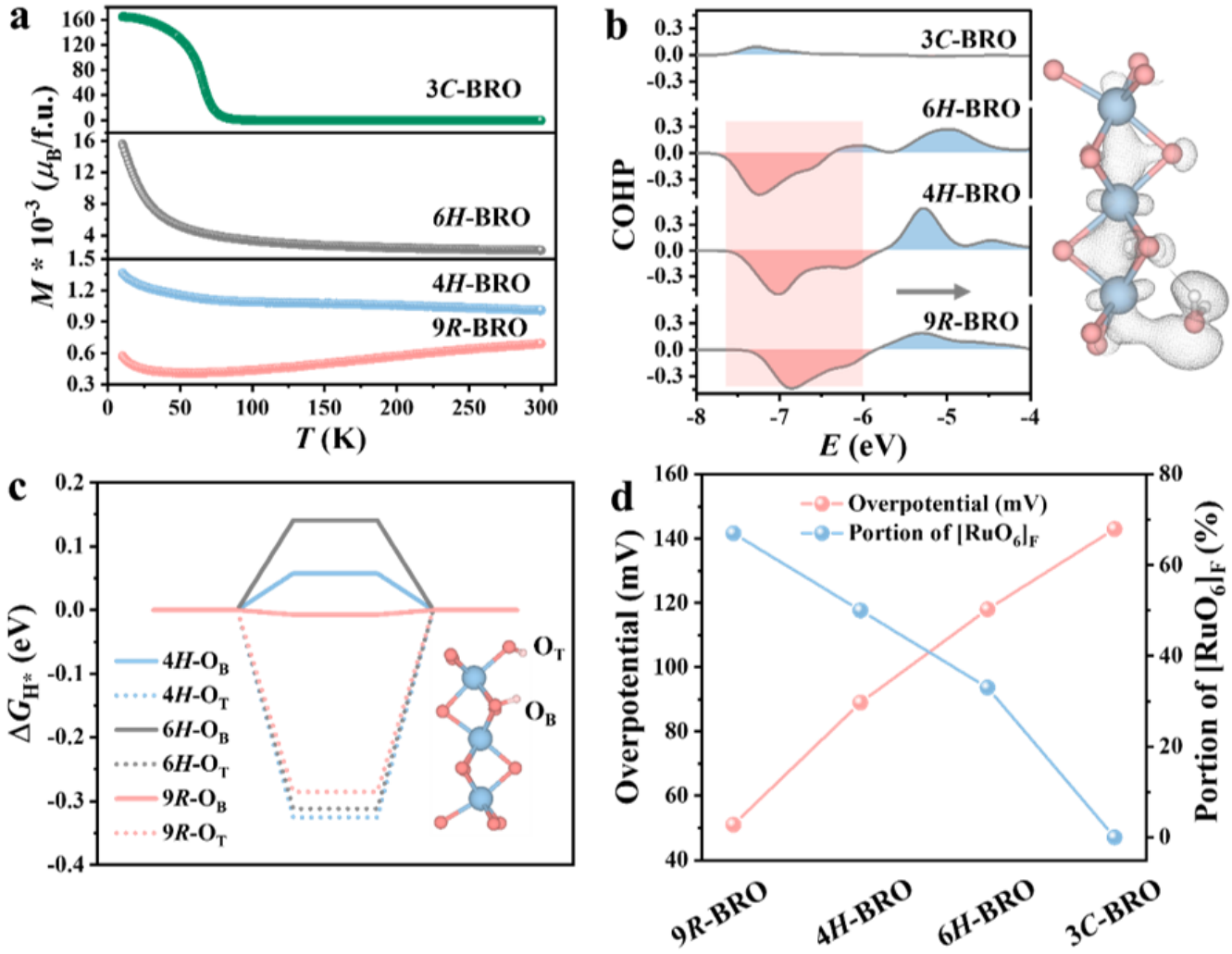

Figure 4

The correlation between crystal structure feature and alkaline HER activity. a, Magnetic behavior of different phases of BRO showing FM (3C-) and AFM (9R-) behavior at 1 Tesla. **b,** Crystal orbital Hamilton populations for face-shared Ru atoms in $BaRuO_3$. The negative value of COHP represent bonding which are shown in pink. Right: Charge density distribution of metal-metal interactions in 9*R*-BRO. **c**, Gibbs energy of H* adsorption on O atoms in face-sharing pose (O_B) and corner-sharing pose (O_T) on different surfaces. **d,** Variation of overpotential at 10 mA cm^{-2} reflecting different proportions of face-shared octahedra in BRO polymorphs.

Supplementary Files

This is a list of supplementary files associated with this preprint. Click to download.

- TOC.png
- SupportingInformation.docx